CRYSTAL GROWTH & DESIGN

Article

Cite This: Cryst. Growth Des. 2019, 19, 5557−5567

pubs.acs.org/crystal

Transformation of Gibbsite to Boehmite in Caustic Aqueous Solution at Hydrothermal Conditions

Xin Zhang,*[,†] Wenwen Cui,[†,‡,§] Jian Zhi Hu,[†] Hsiu-Wen Wang,[∥] Micah P. Prange,[†] Chuan Wan,[†] Nicholas R. Jaegers,[†] Meirong Zong,[†,⊥] Hailin Zhang,[†,‡,§] Carolyn I. Pearce,[†] Ping Li,[‡] Zheming Wang,[†] Sue B. Clark,[†,#] and Kevin M. Rosso*[,†]

[†]Pacific Northwest National Laboratory, Richland, Washington, United States

[‡]Institute of Process Engineering, Chinese Academy of Sciences, Beijing, China

[§]University of Chinese Academy of Sciences, Beijing, China

[∥]Oak Ridge National Laboratory, Oak Ridge, Tennessee 37830, United States

[⊥]School of Earth Sciences and Engineering, Nanjing University, Nanjing, China

[#]Department of Chemistry, Washington State University, Pullman, Washington, United States

Supporting Information

ABSTRACT: Phase transformations among aluminum (oxyhydr)oxide minerals play important roles across a wide range of natural and industrial settings. In highly caustic aqueous solutions, uncertainty persists regarding whether solid-state or dissolution−reprecipitation pathways dominate. We explored the transformation of gibbsite [α-Al(OH)$_3$] to boehmite (γ-AlOOH) in caustic NaOH solution at hydrothermal conditions as a function of temperature, Al(III) and NaOH concentrations, and reaction time. Comparison of detailed structural and morphological solids characterization by X-ray diffraction, scanning electron microscopy/transmission electron microscopy, atomic force microscopy, Raman spectroscopy, and high-field ^{27}Al MAS NMR to predictions from equilibrium thermodynamics calculations suggests the critical importance of dissolution−reprecipitation across our range of system conditions. The yield and physical properties of the boehmite product were found to be sensitive to the hydrothermal treatment temperature and the Al/OH$^-$ ratio, controlled by the loading of gibbsite with respect to NaOH. Experiments at lower Al/OH$^-$ ratios (e.g., 0.64) indicate that the dissolution of the gibbsite reaches an aqueous aluminate saturation state sufficient to overcome the nucleation barrier for boehmite. Higher Al/OH$^-$ ratios (e.g., 3.2) are found to slow the phase transformation, leaving residual unreacted gibbsite in the final product. Higher temperatures appear to improve the phase transformation rate but also typically yield smaller-sized boehmite particles. Particle morphological analyses compared to thermodynamic expectations suggest an important role of kinetics at mineral/solution interfaces, both in the gibbsite dissolution rate as well as the growth rate of boehmite nanocrystals.

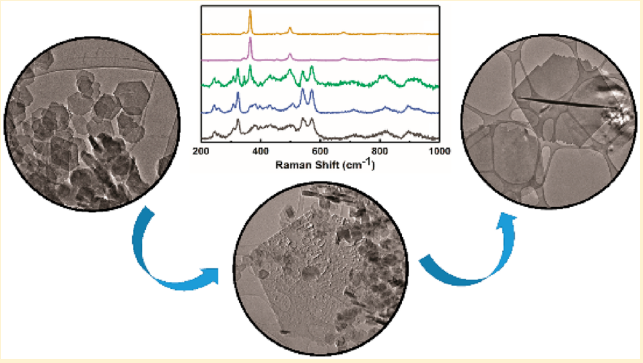

INTRODUCTION

Phase transformations among aluminum (oxyhydr)oxide minerals play important roles across a wide range of natural and industrial settings. For example, the aluminum hydroxide gibbsite [α-Al(OH)$_3$] and aluminum oxyhydroxide boehmite (γ-AlOOH) are dominant precursor phases for the production of aluminum-based materials[1,2] for various industrial applications as adsorbents,[3−5] fire retardants,[6] coatings,[7] catalysts,[8,9] light-emitting diodes (LEDs), and luminescence powders.[10] Such minerals are typically sourced from naturally abundant raw aluminum ore deposits of bauxite[11] by refining its mineralogy of aluminum phases using well-known techniques such as the Bayer process.[12] Furthermore, gibbsite and boehmite are major components of the solids in nuclear processing wastes stored in hundreds of tanks at the Hanford Nuclear Reservation (WA, USA) and at the Savannah River site (SC, USA).[13−16] In this case, challenges in the manipulation of the aluminum inventory are a cost-driver for the development of waste processing and vitrification strategies; concerns include the recalcitrance of boehmite to dissolution, uncontrolled gibbsite precipitation, and phase transformation of gibbsite to boehmite.[15,17,18]

Processing of aluminum ores and nuclear waste, in particular, involve phase transformations in highly caustic

Received: April 8, 2019
Revised: August 4, 2019
Published: August 23, 2019

DOI: 10.1021/acs.cgd.9b00468
Cryst. Growth Des. 2019, 19, 5557−5567

aqueous solutions for which aluminum intermediate species are less well understood compared to that at low pH.[13,19,20] In contrast to predominantly octahedral Al species and clusters in acidic conditions, in caustic solutions aluminum speciation is dominated by the tetrahedral aluminate oxyanion.[21] Reaction fluxes in such solutions appear to involve complex ion pairing/solvent interactions,[21−23] and potentially important but incompletely characterized minor complexes such as aluminate dimers[21−23] and possibly higher order oligomers.[21−23] In the corresponding solids, such as gibbsite and boehmite, aluminum coordination is exclusively octahedral.[24] This suggests a potentially important but still poorly quantified role of aluminum coordination change dynamics at solution/solid interfaces for controlling the kinetics of dissolution, nucleation, and growth processes in caustic solutions.[21−23]

The present study focuses on understanding the transformation of gibbsite to boehmite in concentrated sodium hydroxide solution, with a goal of clarifying the relative importance of solution versus solid-state transformation pathways. The hydrothermal transformation of gibbsite to boehmite can be written simply as

$$Al(OH)_3 \rightarrow AlOOH + H_2O \quad (1)$$

from which both dissolution/reprecipitation and solid-state dehydration pathways may be hypothesized, the latter in particular for concentrated caustic solutions where the water activity is low. Although the crystal structures of gibbsite and boehmite are quite different,[20,25] and therefore a strictly topotactic solid-state transformation pathway likely does not exist, solid-state dehydration leading to local reorganization of the Al−O(H)−Al network topology into the boehmite framework conceptually could circumvent kinetic bottlenecks associated with mass transfer via intermediate aluminate species.

Limited previous work to date is inconclusive with regard to which mechanism is dominant. For example, Panasyuk et al. studied this transformation at 200 and 250 °C in both water vapor and water at circumneutral conditions.[26] They claimed the transformation was a solid-state process, in which water diffusion into the gibbsite structure along the (001) cleavage plane facilitated delamination and dehydration resulting in rapid transformation to boehmite. In strongly caustic solutions under hydrothermal conditions at 150 °C, Gong et al.[18] suggested two transformation mechanisms that appeared to depend on the corresponding pressure. When the reaction container was incompletely sealed, they concluded that boehmite emerged from dehydration and nucleation within gibbsite, as opposed to gibbsite dissolution−boehmite recrystallization when the reaction vessel was completely sealed; in the latter case, the size and morphology of boehmite particles did not show a dependence on the characteristics of the initial gibbsite particles. Both studies relied mainly on X-ray diffraction (XRD), IR spectroscopy, scanning electron microscope (SEM), and transmission electron microscopy (TEM), which precluded important additional clues obtainable from, for example, detailed nuclear magnetic resonance (NMR) spectroscopy directed at following the evolution of surface aluminum coordination change in detail.

Here we use a combination of atomic force microscopy (AFM), SEM, TEM, Raman spectroscopy, and XRD, to add substantial new insight into the transformation mechanism. We systematically explore the effects of temperature, and the absolute and relative concentrations of gibbsite and NaOH, and the reaction duration, on the rate and extent of transformation and the characteristics of solid products. Equilibrium thermodynamic modeling is used to assess the saturation state with respect to product boehmite, to aid data interpretation in terms of possible kinetic effects. We also employ magic-angle spinning nuclear magnetic resonance (MAS NMR) spectroscopy to analyze the solids at various stages of reaction to follow the transformation in terms of Al coordination change; for example, we exploit high fields to enable clear resolution of possible tetra- and intermediate pentacoordinated aluminum sites.

The collective findings show conclusively that the principal transformation mechanism is dissolution−reprecipitation, reinforcing the view of aluminum mass transfer through the caustic solution phase as playing a critical role. We found no convincing evidence for solid-state transformation. Hence, the dynamics of aluminum coordination change between four and six during nucleation and growth is an important consideration with respect to understanding the phase transformation kinetics and the resulting properties of boehmite particles. In this regard, the findings help improve the understanding of processes relevant to both nuclear waste processing as well as development of design strategies for tailored synthesis of boehmite nanomaterials.[25]

EXPERIMENTAL METHODS

Preparation of the Gibbsite. Euhedral hexagonal gibbsite nanoplates were prepared as described elsewhere.[20] Typically, 1 M NaOH (≥98%, Sigma-Aldrich) aqueous solution was added into 0.25 M $Al(NO_3)_3$ (≥98%, Sigma-Aldrich) solution to adjust the solution pH to ∼5. Gel-like precipitates formed during neutralization. After being stirred at room temperature for 1 h, the precipitates were collected by centrifuging and then were washed with deionized water three times. The wet precipitates were dispersed into deionized water and then transferred into a Teflon-lined Parr vessel, which was sealed and reacted at 80 °C for 3 days using a rotation oven with a speed around 10 rpm. The total Al(III) concentration in the reactor was ∼0.25 M. The resulting pure-phase gibbsite precipitates were collected from the Parr vessel, centrifuged, and then washed three times using deionized water. This gibbsite material was characterized by various techniques including XRD, SEM, TEM, and MAS NMR.

Gibbsite−Boehmite Phase Transformation. Gibbsite−boehmite phase transformation experiments were performed using a hydrothermal method: A preselected mass of the synthetic gibbsite particles was dispersed into deionized water and then NaOH was added until the NaOH concentration achieved target values ranging from 0.01−3 M. The suspension was transferred to a 20 mL Teflon-lined Parr vessel. The volume of the solution was 16 mL, and the concentration of Al(III) ions (based on the added gibbsite powders) ranged from 0.064 to 0.64 M. The vessel was sealed and taken to hydrothermal reaction conditions for 6 h to 10 days at either 100, 120, or 200 °C using a rotation oven with a speed around 10 rpm. In some reactions, to explore the effect of secondary additives, partner experiments were performed using either sodium aluminate ($NaAlO_2$), sodium acetate (NaAc), and sodium oleate solutions. The resulting white product was recovered by centrifuging, washed with deionized water three times, and then dried at 80 °C overnight. Samples were characterized by various techniques including XRD, AFM, SEM, TEM, and MAS NMR.

X-ray Diffraction. XRD patterns of gibbsite and boehmite samples were recorded using a Philips X'pert Multi-Purpose diffractometer (MPD) (PANAlytical, Almelo, The Netherlands) equipped with a fixed Cu anode operating at 50 kV and 40 mA. XRD patterns were collected in the range of 5−80° 2θ. Phase identification was performed using JADE 9.5.1 from Materials Data Inc., and the 2012 PDF4+ database from International Center for Diffraction Data (ICDD) database.

DOI: 10.1021/acs.cgd.9b00468
Cryst. Growth Des. 2019, 19, 5557−5567

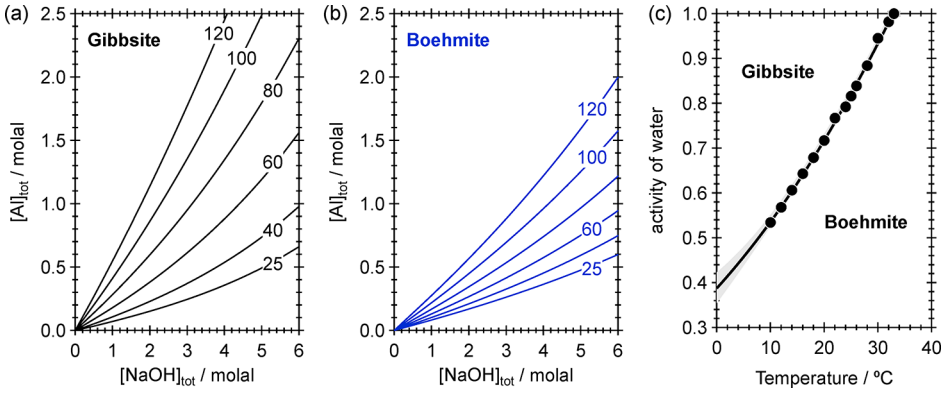

Figure 1. PHREEQC calculations for the solubility of (a) gibbsite, (b) boehmite, and (c) their interconversion in NaOH solutions at temperatures up to 120 °C. In plot (c), a third-order polynomial curve fitting (solid line) with 95% confidence intervals (gray area) are shown as a guide to the eye. See ref 28 for PHREEQC data block code.

Table 1. Overview of Boehmite Synthesis Conditions and Resulting Products

entry	concentration of Al^{3+} (M, based on added gibbsite)	concentration of NaOH (M)	temp (°C)	time	product	equilibrium calculation (saturation index/ SI)[a] gibbsite	boehmite
1	0.256	0.2	100	10 days	boehmite	0.00	0.38
2	0.256	0.2	120	7 days	boehmite	0.00	0.49
3	0.256	0.2	200	2 days	boehmite		
4	0.256	0.01	120	3 days	gibbsite	0.00	0.49
5	0.256	0.1	120	3 days	boehmite	0.00	0.49
6	0.256	0.2	120	3 days	boehmite	0.00	0.49
7	0.256	0.5	120	3 days	N/A	−0.04	0.45
8	0.256	1	120	3 days	N/A	−0.54	−0.04
9	0.256	3	120	3 days	N/A	−1.17	−0.64
10	0.064	0.1	100	10 days	gibbsite + boehmite	0.00	0.38
11	0.064	0.2	100	10 days	N/A	−0.14	0.24
12	0.064	0.1	120	7 days	boehmite	0.00	0.49
13	0.064	0.2	120	7 days	N/A	−0.38	0.11
14	0.256	0.1	100	10 days	boehmite	0.00	0.38
15	0.256	0.1	120	7 days	boehmite	0.00	0.49
16	0.64	0.2	100	10 days	gibbsite + boehmite	0.00	0.38
17	0.64	0.5	100	10 days	boehmite	0.00	0.38
18	0.64	0.2	120	7 days	boehmite	0.00	0.49
19	0.64	0.5	120	7 days	boehmite	0.00	0.490
20	0.256	0.2	120	6 h	gibbsite	0.00	0.49
21	0.256	0.2	120	24 h	97% gibbsite + 3% boehmite	0.00	0.49
22	0.256	0.2	120	30 h	70% gibbsite + 30% boehmite	0.00	0.49
23	0.256	0.2	120	36 h	boehmite	0.00	0.49
24	0.256	0.2	120	42 h	boehmite	0.00	0.49
25	0.256	0.2	120	48 h	boehmite	0.00	0.49

[a]In order to demonstrate the extent of supersaturations with respective to (w.r.t.) boehmite, all calculations were forced to be equilibrated based on gibbsite solubility. That is the target $SI_{gibbsite}$ = 0.0 whenever possible, and therefore, a negative $SI_{gibbsite}$ value means that the target saturation cannot be attained due to insufficient amounts of gibbsite in the initial solution assemblage. The saturation index w.r.t. gibbsite is defined as $SI_{gibbsite} = \log[a_{Al(OH)_4}/(a_{OH^-}K_{s4})]$, where K_{s4} (derived from the Pizer model) = 10−0.18 and 100.05 (at 100 and 120 °C, respectively). The saturation index w.r.t. boehmite is defined as $SI_{boehmite} = \log[a_{Al(OH)_4}a_H/(K_{s4})]$, where K_{s4} (derived from the Pizer model) = 10−12.78 and 1012.39 (at 100 and 120 °C, respectively). In the Supporting Information, we provided an example for the PHREEQC input file for experiment entries **4**−**9**.

Atomic Force Microscopy (AFM). The thickness and morphology of gibbsite and boehmite samples were measured using a Dimension Icon AFM (Bruker, USA) operated in contact mode. All images were collected using silicon nitride tips with backside Au reflective coating (MLCT, Bruker, USA) at a scan rate of 1 Hz with 512 × 512 lines scan. AFM samples were mounted by drop-casting sample suspensions onto silicon substrates (Nova Electronic Materials Ltd.), and then the excess was blown off after 30 min with a stream of N_2 gas. Mounted samples were washed several times using DI water and dried using N_2 gas. Note: Prior to sample mounting, silicon substrates were cleaned in DI water via sonication twice and then sonicated in ethanol. Finally, silicon substrates were cleaned using a

DOI: 10.1021/acs.cgd.9b00468
Cryst. Growth Des. 2019, 19, 5557−5567

plasma cleaner for 30 min under Ar atmosphere followed by an ozone cleaner for 30 min.

Scanning Electron Microscopy. The morphologies of gibbsite and boehmite samples were investigated by using a Helios NanoLab 600i SEM (FEI, Hillsboro, OR). Approximately around 5 nm of carbon was sputter-coated on all samples to enhance the imaging behavior.

Transmission Electron Microscopy. The morphologies of gibbsite and boehmite samples were also investigated by using a TEM (FEI Titan TEM). Samples for TEM measurements were made by dropping sample suspensions onto copper grids (Lacey Carbon, 300 mesh, Copper grid, Ted Pella, Inc.) which were then allowed to dry in air under ambient conditions. TEM was performed with an acceleration voltage of 300 kV. AFM, SEM, and TEM were also used to evaluate the size distribution of synthetic gibbsite and boehmite.

NMR Spectroscopy. Single-pulse ^{27}Al MAS NMR experiments were performed at room temperature (~20 °C) on a Varian-Inova 850 MHz NMR spectrometer using a commercial 3.2 mm pencil-type probe and operating at a magnetic field of 19.975 T and sample spinning rate of 20 kHz. The corresponding ^{27}Al Larmor frequencies were 221.413 MHz. For ^{27}Al MAS NMR acquisitions, a single-pulse sequence with a pulse width of 0.5 μs (corresponding to a solid $\pi/4$ pulse) and a ^{27}Al radio frequency (rf) field strength of 83.3 kHz [i.e., 3.0 μs for a liquid $\pi/2$ pulse that was calibrated by using 1 M $Al(NO_3)_3$ aqueous solution] were used. Each spectrum was acquired using a recycle delay time of 1 s, which is sufficiently long to allow all the magnetization to return to its equilibrium state, and an acquisition time of 20 ms. Chemical shifts were referenced to 1 M $Al(NO_3)_3$ aqueous solution (0 ppm). Both hydrated and dehydrated ^{27}Al MAS NMR spectra were collected with 3000 scans.

Equilibrium Thermodynamics Calculations. Equilibrium thermodynamics calculations were performed using the code PHREEQC with the Pitzer database.[27] The details of these calculations and the PHREEQC input data block can be found in our previous work.[28]

RESULTS AND DISCUSSION

Equilibrium Thermodynamics of System Conditions. We first developed predictions based on thermodynamic modeling to assess the saturation state of our system with respect to gibbsite conversion to boehmite, according to eq 1, at our chosen Al and NaOH concentrations, and run temperatures. Equilibrium thermodynamics calculations were performed using the code PHREEQC with the Pitzer database[27] using our prior tabulated data block[28] applied to each specific experimental condition in the present study (except for the 200 °C experiments where the reliable thermodynamic data is limited). Pitzer models for the thermodynamics of sodium aluminate solutions and the solubility of gibbsite and boehmite in the $Al(OH)_3$-NaOH-H_2O system have been reported previously by various authors.[29−34] In our related work[28] prior to the present study, we constructed the PHREEQC[27] data block code using equilibrium constants and Pitzer parameters selected from the literature, and subsequent calculations were verified by comparing model predictions to literature data.

Using this code to model the experimental conditions in the present study, we obtained the gibbsite and boehmite solubility results shown in Figure 1a,b. In comparing the relative stabilities of the two phases, the stability of boehmite with respect to gibbsite increases with temperature and the concentration of NaOH, as evidenced by the increasing difference in their solubility. As shown in Table 1, for most of our experimental conditions, the system is less stable with respect to gibbsite and more stable with respect to boehmite; we therefore expect gibbsite to transform to boehmite in most cases. Our calculations also predict that in the $Al(OH)_3$−NaOH−H_2O system, gibbsite is the solubility limiting phase below ~33 °C at water activity of 1 (i.e., infinitely dilute), but boehmite becomes more stable than gibbsite on lowering water activity (Figure 1c).

Effect of Reaction Temperature. To help provide a basis for interpreting observed characteristics of product solids in terms of growth mechanism, experiments were designed to systematically test the effects of the reaction temperature, the Al(III) precursor concentration, and the NaOH concentration. As shown in Table 1 (entries **1**−**3**), three temperatures of 100, 120, and 200 °C were investigated at fixed Al(III) precursor and NaOH concentrations of 0.256 and 0.2 M, respectively. The reaction time was 10 days, 7 days, and 2 days for 100, 120, and 200 °C reactions, respectively, selected to give sufficient time for complete conversion to boehmite.

For these temperature-dependent experiments, all cases were predicted or, in the case of the 200 °C run which could not be directly modeled, were expected to be variably supersaturated with respect to boehmite (Table 1, entries **1**−**3**). On the basis of Figure 1a,b, we expect an increasing thermodynamic driving force to boehmite with increasing temperature. As shown in Figure 2, XRD showed samples resulting from all reactions

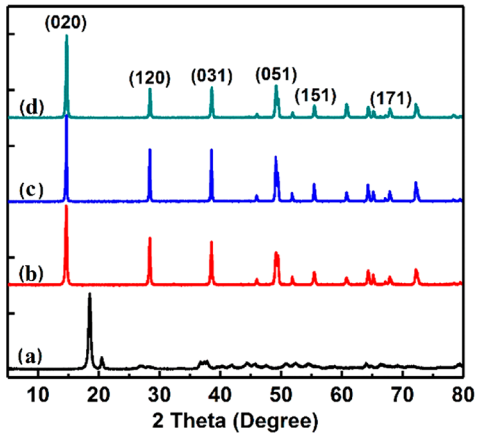

Figure 2. XRD patterns of precursor gibbsite and product boehmite produced at different hydrothermal reaction conditions. (a) Gibbsite; (b) 100 °C, 10 days; (c) 120 °C, 7 days; (d) 200 °C, 2 days. The concentration of gibbsite and NaOH is 0.256 and 0.2 M, respectively.

were pure boehmite, in agreement with expectations. The diffraction pattern was in good agreement with reference data (ICDD PDF # 00-74-1895).[25] The strong diffraction peak at the 2θ angle of 14.5 was readily assignable to (020) diffraction.

The morphology of product boehmite was of particular interest with respect to gaining insight into the kinetics of growth and the mechanism of transformation. Nominally, particle morphologies depend on their surface energetics, particularly when growth occurs near equilibrium, so as to minimize the total surface free energy.[35] However, the effect of kinetics can also be important, especially when highly supersaturated and growth occurs far from equilibrium. It is noteworthy that boehmite particles are known to show remarkably varied morphologies, depending on synthesis factors such as solution pH, precursor types and concentrations, and reaction temperatures.[25,36−40]

SEM, TEM, and AFM showed that all boehmite products tended to conform to plate-like shapes, with the dominant surface being (010) (Figure 3, **4** and **5**). Furthermore,

DOI: 10.1021/acs.cgd.9b00468
Cryst. Growth Des. 2019, 19, 5557−5567

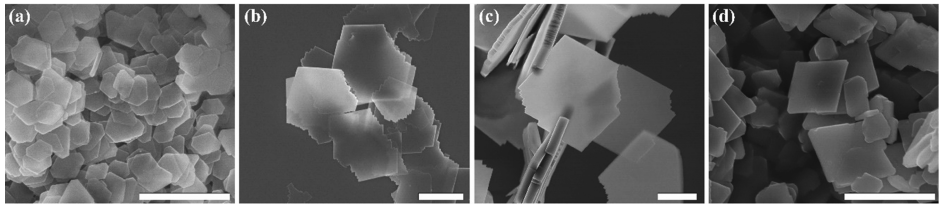

Figure 3. SEM images of precursor gibbsite and product boehmite produced at different temperatures. (a) Gibbsite; (b) 100 °C, 10 days; (c) 120 °C, 2 days; (d) 200 °C, 2 days. The concentration of gibbsite and NaOH is 0.256 and 0.2 M, respectively. The scale bar is 1 μm.

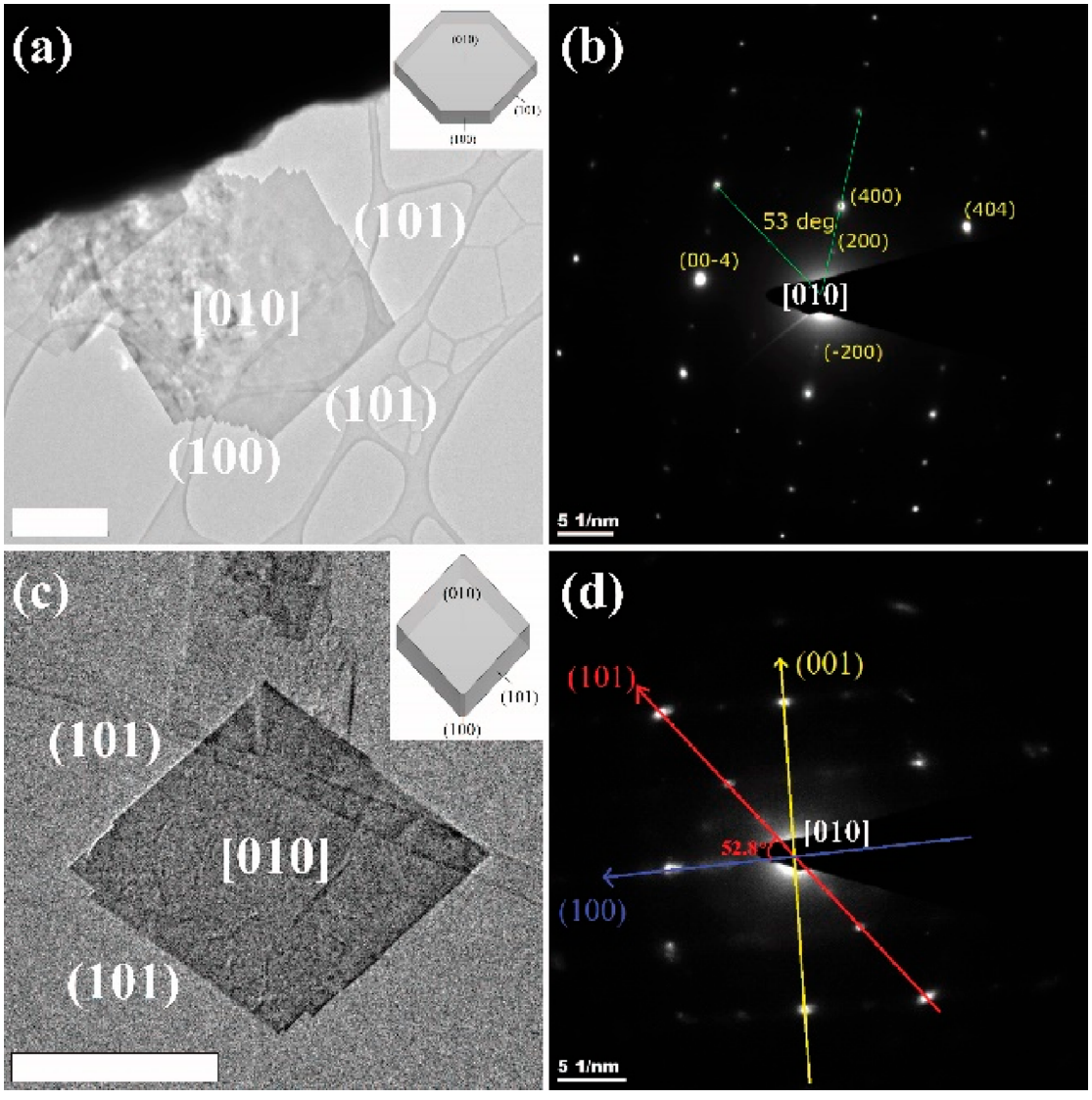

Figure 4. TEM images of boehmite produced at (a and b) 120 °C, 2 days and (c and d) 200 °C, 2 days, showing hexagonal and rhombic particle shapes. The concentration of gibbsite and NaOH is 0.256 and 0.2 M, respectively. The scale bar is 1 μm.

boehmite platelets from lower temperatures (100 and 120 °C) exhibited a uniform hexagonal edge morphology, whereas the boehmite platelets from the highest temperature run exhibited a rhombic shape. Intriguingly, this subtle distinction in platelet edge terminations may reflect a stronger influence of kinetics in the lower temperature runs, as opposed to the more highly supersaturated highest temperature run.

For example, previous density functional theory (DFT) calculations suggest that in caustic conditions similar to ours, the surface energies of the four main low-index boehmite surfaces, including (001), (100), (101), and (010), are approximately 0.90, 0.57, 0.39, and 0.28 J·m^{-2}, respectively.[35] The (010) face is predicted to have the lowest surface energy, making it the most probable to manifest for growth near equilibrium, consistent with our observations of (010)-dominant platelets. In contrast, the large surface energy of (001) makes this edge termination the least likely to appear. And the somewhat larger surface energy of (100) relative to (101) suggests that near-equilibrium growth should favor (101) edges, followed by (100). This would tend to produce platelets with a rhombic set of edge terminations, while introduction of (100) edges would manifest as hexagonal

DOI: 10.1021/acs.cgd.9b00468
Cryst. Growth Des. 2019, 19, 5557−5567

truncations of the rhombic margin.[35] While the latter is consistent with our morphology observations for the lower temperature boehmites (100 and 120 °C), close examination of the nominally (100)-oriented edges shows that these are actually vicinal surfaces comprised of alternating lower energy (101) nanofacets, as shown in SEM (Figure 3b,c), TEM (Figure 4a), and AFM images (Figure S1). It thus appears that rhombic-shaped platelets reflecting the predicted equilibrium growth morphology were enabled by the highest temperature (200 °C) conditions, perhaps because at this temperature the growth rate along the [100] direction was sufficiently fast to eliminate (100) edge facets. As shown in SEM (Figure 3b–d), TEM (Figure 4), and AFM images (Figure S1), the sizes (along the [100] direction, $L_{[100]}$) of the boehmite synthesized at 100, 120, and 200 °C are 2–6 μm, 1–5 μm, and 0.2–1 μm, respectively; and the thicknesses (along the [010] direction, $L_{[010]}$) of the boehmite synthesized at 100, 120, and 200 °C are 60–100 nm, 40–100 nm, and 20–160 nm, respectively, The corresponding aspect ratio of $L_{[100]}/L_{[010]}$ changes from 33/1–60/1, 25/1–50/1 to 10/1–6/1, which indicated that a higher temperature enhanced growth of boehmite along the [010] direction to form thicker products.

Effect of NaOH Concentration. Next, we examined the effect of the NaOH concentration, while fixing the gibbsite precursor concentration to 0.256 M, the temperature at 120 °C, and the run duration at 3 days. We investigated six different concentrations of NaOH at 0.01, 0.1, 0.2, 0.5, 1.0, and 3.0 M, as shown in Table 1 (entries **4**–**9**). Calculated saturation index (SI) values for gibbsite and boehmite were both less than 0 when the concentrations of NaOH were 1.0 and 3.0 M (Table 1, entries **8** and **9**), thus predicting complete dissolution of gibbsite and no product boehmite. Indeed, in our experiments at these conditions no solid phase product was recovered. Thermodynamic modeling further suggested a stable boehmite product should form for the remaining four lower NaOH concentrations (Table 1, entries **4**–**7**). However, we observed no solid product from the experiment at the intermediate concentration of 0.5 M NaOH, apparently a transitional saturation state in which thermodynamic equilibrium may be difficult to achieve within 3 days.

For the remaining three NaOH concentrations, solids were recovered. As shown in Figure S2, XRD patterns indicated that samples produced using 0.1 and 0.2 M NaOH were pure boehmite, but the solids collected using the lowest concentration of 0.01 M NaOH were pure residual gibbsite. On this latter material, dissolution features were clearly observable at the resolution of SEM imaging (Figure 5a), consistent with the thermodynamic prediction of gibbsite instability. However, no evidence for boehmite nucleation was obtained, again likely because of slow kinetics, in this case due to slow dissolution of gibbsite and not achieving the desired saturation state with respect to boehmite. From the 0.1 and 0.2 M NaOH systems, SEM imaging (Figure 5b,c) showed that the boehmite products were hexagonal-shaped platelets, with growth morphology considerations discussed above relevant to these experimental results in the same manner (e.g., except for its shorter run duration, the 0.2 M experiment is identical to run #2, Table 1).

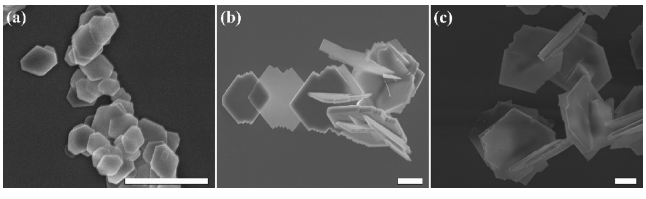

Figure 5. SEM images of product boehmite produced at (a) 0.01 M; (b) 0.1 M; and (c) 0.2 M NaOH. The temperature and reaction time for all reactions were 120 °C and 3 days, respectively. The concentration of the precursor gibbsite was 0.256 M. The scale bar is 1 μm.

Collectively, this series of NaOH concentrations revealed an apparently significant nucleation barrier for boehmite. The slow gibbsite dissolution rate at 0.01 M NaOH precluded the aluminate concentration in solution from increasing sufficiently within the duration of the experiments to induce boehmite nucleation and crystallization. The nucleation barrier may be relatively large given complete gibbsite dissolution in the higher concentration experiments that are also predicted to be within the boehmite stability field, though boehmite only appeared in the 0.1 and 0.2 M NaOH solutions. Furthermore, the presence of gibbsite surfaces does not appear to catalyze nucleation and growth of boehmite.

Effects of Precursor Concentration and the Ratio of Gibbsite to NaOH. To gain a better understanding of the role of Al/OH^- ratio on boehmite nucleation and growth, through its control of the extent of departure from equilibrium, we augmented the above set of experiments with runs using 0.064, 0.256, and 0.64 M gibbsite with respect to the NaOH concentration. This was done for three NaOH concentrations of 0.1, 0.2, and 0.5 M, and two temperatures of 100 and 120 °C, using reaction times of 10 days for 100 °C and 7 days for 120 °C, respectively (Table 1, entries 1, 2, **10**–**19**). Thermodynamic calculations predict complete conversion of gibbsite to boehmite in all such experiments.

Four experiments were performed with a gibbsite concentration of 0.064 M. No boehmite formed in 0.2 M NaOH solution at both 100 and 120 °C despite complete gibbsite dissolution (Table 1, entries **11** and **13**). In both cases, the corresponding aluminate concentration of 0.064 M appears insufficient to nucleate boehmite. Using the same gibbsite concentration and run duration, but in 0.1 M NaOH solution, boehmite formed at both 100 and 120 °C (Table 1, entries **10** and **12**). Hence, this higher Al/OH^- ratio appears to enhance boehmite nucleation and growth, and, conversely, excess NaOH appears disruptive to boehmite nucleation at these conditions. It is noteworthy, however, that at 0.1 M NaOH a 0.064 M aluminate solution was achieved only at 120 °C (Figure S3a). As shown in Figure 6a, residual gibbsite was present at 100 °C (Table 1, entry **10**). At this condition, the boehmite yield was low (only 10% of the Al concentration was recovered as solids, some of which was residual gibbsite), suggesting very slow transformation but with conditions sufficient to overcome the energy barrier to nucleate boehmite. At 120 °C (Table 1, entry **12**), the boehmite yield was much higher, and correspondingly larger crystallites grew, albeit in this case with more morphologically irregular particles (Figure 6b). In addition, the average size of the boehmite collected from the 120 °C system was found to be smaller than that from the 100 °C system (Figure 6a). Particle size can be taken as approximately proportional to the nucleation/growth rate. Higher temperatures can promote both crystal growth and the nucleation rate. As a result, pure boehmite with much higher yield formed, but the size was smaller. Collectively, the results of these four experiments reflect the importance of the Al/

DOI: 10.1021/acs.cgd.9b00468
Cryst. Growth Des. 2019, 19, 5557–5567

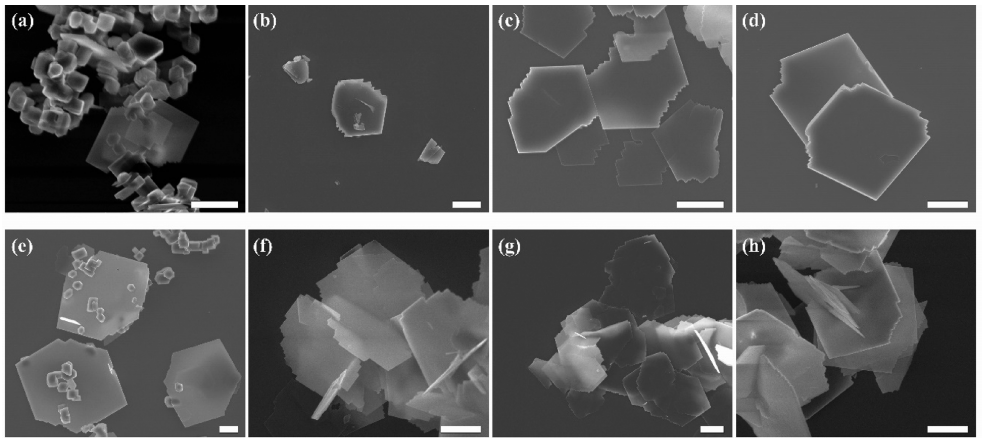

Figure 6. SEM images of product boehmite produced at (a) 0.064 M gibbsite, 0.1 M NaOH, 100 °C; (b) 0.064 M gibbsite, 0.1 M NaOH, 120 °C; (c) 0.256 M gibbsite, 0.1 M NaOH, 100 °C; (d) 0.256 M gibbsite, 0.1 M NaOH, 120 °C; (e) 0.641 M gibbsite, 0.2 M NaOH, 100 °C; (f) 0.641 M gibbsite, 0.2 M NaOH, 120 °C; (g) 0.641 M gibbsite, 0.5 M NaOH, 100 °C; and (h) 0.641 M gibbsite, 0.5 M NaOH, 120 °C. The reaction time was 10 days and 7 days for 100 and 120 °C. The scale bar is 1 μm.

OH^{--} ratio for controlling the stability field of boehmite, generally indicating that values larger than 0.64 are necessary to overcome the nucleation barrier.

Increasing the precursor gibbsite concentration to 0.256 M, pure boehmite was produced in both 0.1 and 0.2 M NaOH solution at both 100 and 120 °C (Figures 2a,b and S3b,3c). SEM showed that all produced boehmites were hexagonal platelets with sizes larger than 1 μm (Figures 3a,b and 6c,d). In all cases, here the Al/OH^- ratio is larger than 1.28. When the concentration of gibbsite was increased further to 0.64 M, pure boehmite was produced in both 0.2 and 0.5 M NaOH solution at 120 °C (Figure S3e,g) and 0.5 M NaOH solution at 100 °C (Figure S3f); however, unreacted gibbsite was detected in the 0.2 M NaOH solution at 100 °C (Figure S3d). SEM showed all resulting boehmites were uniform hexagonal platelets larger than 1 μm (Figure 6e–h). It thus appears that once the Al/OH^- ratio is sufficient to result in boehmite crystallization, increasing it further does not have a noticeable impact on crystal size. In fact, there was no obvious change in crystal size with increasing precursor concentration, NaOH concentration, and/or the ratio of gibbsite to NaOH once boehmite crystallization commenced.

Crystal Growth Mechanisms. To better understand the transformation mechanism, we examined the evolution of the solid phases over time using an otherwise fixed set of reaction conditions (Table 1, entries **20**–**25**). For the reaction time of 6 h, XRD showed pure residual gibbsite was collected (Figure S4a), and SEM (Figure 7a), TEM (Figure 8a), and AFM (Figure S5) images showed dissolution features on these particles. This reinforces the finding that gibbsite dissolution precedes boehmite crystallization at these conditions, conceptually consistent with a dissolution–reprecipitation mechanism rather than a solid-state transformation pathway (i.e., dehydration). At 24 h, XRD showed a mixture of 97% gibbsite and 3% boehmite (Figure S4b), although the boehmite was not readily detectable by SEM (Figure 7b) or TEM (Figure 8b). There was also no evidence of boehmite nuclei on residual gibbsite surfaces. At 30 h, XRD showed a mixture of 70% gibbsite and 30% boehmite (Figure S4c), while both SEM (Figure 7c) and TEM (Figure 8c) showed some microsized hexagonal boehmite platelets among residual gibbsite. Although irregularly shaped, boehmite platelets were always structurally distinct from gibbsite, and there was no evidence suggesting they were the product of solid-state transformation.

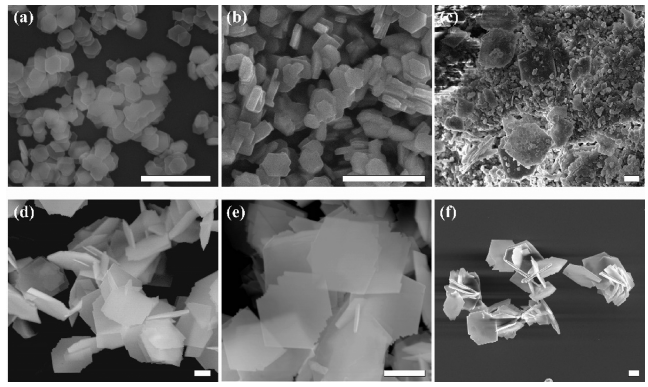

Figure 7. SEM images of samples synthesized at different hydrothermal treatment times: (a) 6 h; (b) 24 h; (c) 30 h; (d) 36 h; (e) 42 h; and (f) 48 h. The concentration of gibbsite and NaOH was 0.256 and 0.2 M, respectively. The temperature was 120 °C. The inset scale bar is 1 μm.

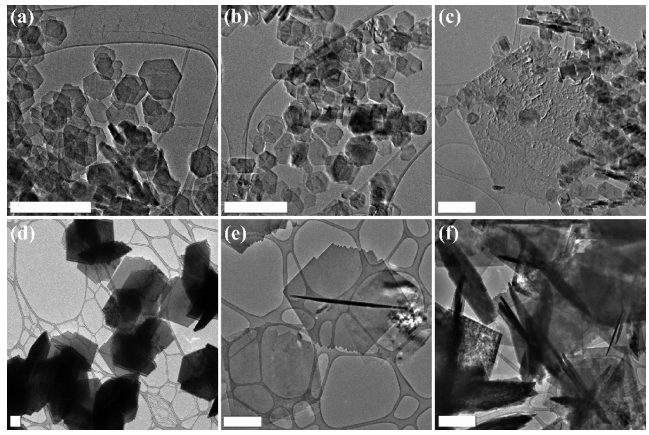

Figure 8. TEM images of samples synthesized at different hydrothermal treatment times: (a) 6 h; (b) 24 h; (c) 30 h; (d) 36 h; (e) 42 h; and (f) 48 h. The concentration of gibbsite and NaOH was 0.256 and 0.2 M, respectively. The temperature was 120 °C. The inset scale bar is 1 μm.

DOI: 10.1021/acs.cgd.9b00468
Cryst. Growth Des. 2019, 19, 5557–5567

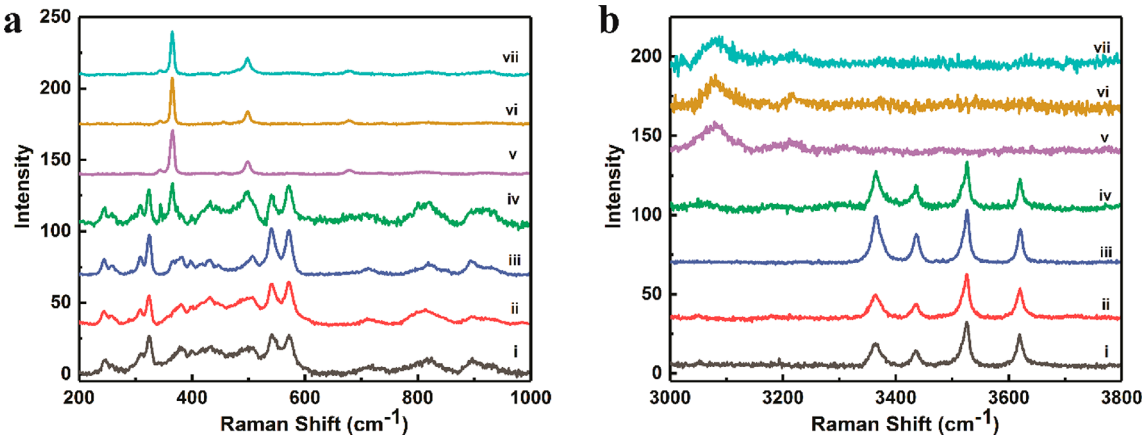

Figure 9. Raman spectra (a) low-wavenumber region and (b) high-wavenumber region of gibbsite and samples synthesized at different hydrothermal treatment times: (i) original gibbsite; (ii) 6 h; (iii) 24 h; (iv) 30 h; (v) 36 h; (vi) 42 h; and (vii) 48 h. The concentration of gibbsite and NaOH was 0.256 and 0.2 M, respectively. The temperature was 120 °C.

Boehmite nucleation therefore occurs in solution. For reaction times longer than 36 h, only pure boehmite was found by XRD (Figure S4d–f), and SEM (Figure 7d–f) and TEM (Figure 8d–f) images showed these were microsized hexagonal platelets.

Characterization by Raman spectroscopy was performed on this time-dependent series in an attempt to detect changes at the level of interatomic bonding during the transformation (Figure 9). Peaks in the Raman spectra of gibbsite and boehmite were mainly detected in the low-wavenumber region from 200 to 1000 cm^{-1} and the high-wavenumber region from 3000 to 3800 cm^{-1}. For gibbsite, the predominant low-wavenumber peak at ~320 cm^{-1} is attributed to Al–O stretching vibrations, and peaks at ~540 and 570 cm^{-1} are attributed to Al–O–Al deformation [Figure 9a(i)];[41−43] four high-wavenumber peaks at ~3615, 3520, 3430, and 3360 cm^{-1} are attributed to hydroxyl stretching υ(OH) [Figure 9b-b(i)].[41−43] For boehmite, the very strong and sharp low-wavenumber peak at ~366 cm^{-1} and another strong peak at ~495 cm^{-1} are attributed to the Al–O stretching vibrations, and the peak at 675 cm^{-1} is attributed to the Al–O–Al deformation [Figure 9a(vii)];[41,43] two broad peaks in the high-wavenumber region located at ~3085 and 3220 cm^{-1} are attributed to hydroxyl stretching υ(OH) [Figure 9b(vii)].[41,43] The Raman data thus can distinguish the two phases, similar to the XRD information, but also go further in that they can reveal possible contributions from structural defects in the bulk or, at a sufficiently high surface area to volume ratio (i.e., small particle sizes), from surface structures.

Compared to the 6 h Raman spectra [Figure 9a(ii) and 9b(ii)], in the 24 h sample a new peak emerges at ~366 cm^{-1} consistent with initial formation of boehmite [Figure 9a(iii)], and this is substantially more intense in the 30 h sample, which also shows new peaks in the high-wavenumber region [Figure 9a(iv) and 9b(iv)]. Only pure boehmite is detected by Raman at longer reaction times [Figure 9a(v)–(vii) and 9b(v)–(vii)], consistent with XRD.

Because nominally the high-wavenumber region was expected to be more sensitive to phase discrimination due to its close ties to the hydrogen bonding structure, the earliest emergence of the peak near 366 cm^{-1} was curious. Visual examination of calculated long-wavelength boehmite vibrational mode eigenvectors indicates that this mode is associated with vibrations involving in-plane motions of the O sublattices relative to the Al sublattice that do not involve the H atoms which are all involved in interlayer bonding. Examination of the evolution of the OH-stretch region of the Raman spectrum above 3000 cm^{-1} shows that the appearance for the first time of the 366 cm^{-1} peak is accompanied by a decrease in intensity of the two highest frequency peaks (~3523 and 3621 cm^{-1}), which corresponds to stretches of the bonds of the intralayer H atoms in gibbsite. Taken together, this evidence suggests that the 366 cm^{-1} peak is indicative of Al–O layers free of intralayer hydrogen bonds and that by 30 h of reaction time a significant amount of intralayer hydrogens have been removed, while the gibbsite framework remains intact.

^{27}Al magic-angle spinning nuclear magnetic resonance spectroscopy (MAS NMR) was also performed on these samples to probe the transformation process at the level of local coordination environment around Al. Figure 10 shows the center band ^{27}Al MAS NMR spectra for these time-dependent samples, corresponding to spectra acquired from the initial state (gibbsite, Figure 10a) to progressively longer reaction times until complete conversion to boehmite (6–42 h, Figure 10b–f). The spectrum of gibbsite (Figure 10a) is comprised of a major peak located at about 11.3 ppm, and two low intensity peaks located at 41.7 and 74.8 ppm, respectively. Gibbsite adopts a hexagonal crystal structure, comprised of quasi two-dimensional $Al(OH)_3$ layers each having two-thirds of the Al_O occupied, and sheets are weakly bound together along the *c*-axis by hydrogen bonding. On the basis of our prior high-field ^{27}Al MAS work on gibbsite,[24] these peaks are assigned to octahedral aluminum coordination (Al_O) (11.3 ppm), pentahedral aluminum coordination (Al_P) (41.7 ppm), and tetrahedral aluminum coordination (Al_T) (74.8 ppm), respectively. Both the Al_P and Al_T are undercoordinated Al sites that reside on gibbsite surfaces,[24] representing structural incompleteness in the form of defects. They are likely concentrated at edge surfaces, given that these are the fast growth directions, and they are nominally the active sites during both growth and dissolution. Hence, generally, a smaller proportion of Al_P and Al_T sites is consistent with more perfect crystallites, whereas a higher proportion could indicate a transitional state (e.g., dissolution).

While we observed a small proportion of Al_P (0.40%) and Al_T (0.09%) sites in the original gibbsite precursor material (Figure 10a), this proportion increases significantly after 6 h reaction to 0.98% Al_P and 0.61% Al_T (Table S1), consistent

DOI: 10.1021/acs.cgd.9b00468
Cryst. Growth Des. 2019, 19, 5557–5567

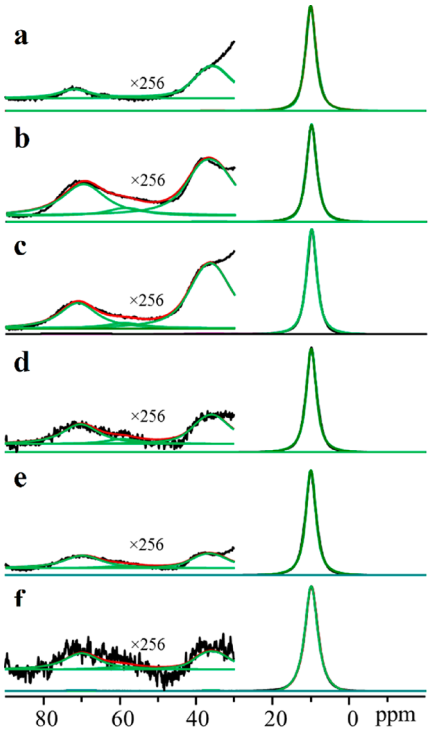

Figure 10. Quadrupolar line shape simulated 1D ^{27}Al MAS NMR spectra of gibbsite and samples synthesized at different hydrothermal treatment times: (a) original gibbsite; (b) 6 h; (c) 24 h; (d) 30 h; (e) 36 h; and (f) 42 h. The concentration of gibbsite and NaOH was 0.256 and 0.2 M, respectively. The temperature was 120 °C. The green lines indicate deconvoluted peaks; solid red lines are simulated overall spectra; solid black lines are experimental spectra.

with gibbsite dissolution during the initial stage of transformation. These defect site proportions appear to remain constant until a dramatic decrease of both Al_T and Al_P in the 30 and 36 h samples, consistent with nearly defect-free boehmite. A caveat is that the surface area of product boehmite is likely much lower than that of initial gibbsite, such that an equivalent concentration of defect sites in product boehmite per unit surface area cannot be ruled out. However, the half -width of the ^{27}Al NMR peak for Al_O decreases with increasing progression toward boehmite (Figure 10e,f), consistent with formation of a more highly crystalline product.

The collective characterization results on the time-dependent series are fully consistent with a dissolution−reprecipitation mechanism for the transformation of gibbsite to boehmite; solid-state transformation would have shown evidence detectable by either TEM or the local structure spectroscopies of the development of mosaic crystallites comprised of mixed gibbsite/boehmite domains. The main transformation steps are (1) gibbsite dissolution releasing primarily aluminate oxyanions into solution, which then (2) accumulate to sufficient concentrations with respect to hydroxyl to then (3) surmount the homogeneous nucleation barrier of boehmite and (4) condense out of solution enabling continuous crystallization of boehmite nanoplates.

Given the evidence for the dissolution−reprecipitation pathway, it was of interest to explore the effects of additives, such as a secondary precursor or simple organic ligands.[44−46] As shown in Table S2 (entry **1** and **2**), sodium aluminate ($NaAlO_2$) solution was used as a secondary precursor additive introduced into the 6 h and 24 h reaction solutions (Table 1, Entry **20** and **21**, respectively), which were then run at 120 °C for another 48 h. XRD patterns indicated products resulting from both reactions were mixtures of gibbsite and boehmite (Figure S6a,b), which included 19.4% and 81.3% boehmite, respectively. For the same reaction conditions without an added secondary Al(III) precursor, the precursor gibbsite transformed to boehmite completely (Table 1, Entry 25), which indicates that addition of the secondary Al(III) precursor decreases the transformation rate of gibbsite to boehmite. SEM showed that boehmite formed in both reactions had morphologies similar to that resulting from the pure gibbsite precursor, but the resulting gibbsite component was bar-shaped, grown from the secondary Al(III) precursor.

As shown in Table S2 (entry **3**−**6**), NaAc and sodium oleate were used as organic ligands additives introduced into 6 and 24 h reaction solutions (Table 1, Entry **20** and **21**, respectively) and then run at 120 °C for another 48 h. XRD patterns indicated products resulting from all of these ligand-modified reactions were mixtures of gibbsite and boehmite (Figure S6c−f), which indicated that organic ligands could also significantly reduce the gibbsite-to-boehmite transformation rate. A total quench of the reaction was not observed however. SEM showed that boehmite formed in NaAc-added reactions had a morphology similar to that formed without it. In contrast, the sodium oleate-added reactions produced boehmite with a leaf-like morphology with round edge surfaces, which indicated that oleate ions could adsorb on the surface of boehmite and thereby influence its crystal growth habit. All of these exploratory tests further reinforced the conclusion that the transformation of the gibbsite to boehmite is a dissolution−reprecipitation process.

CONCLUSIONS

We have investigated the phase transformation of gibbsite to boehmite in caustic hydrothermal environments in detail, comparing experimental observations on solid products with predictions from equilibrium thermodynamic calculations of the saturation state at each set of conditions. On the basis of various XRD and various microscopic and spectroscopic probes including SEM. TEM, AFM, Raman, and high field ^{27}Al MAS NMR, we propose a dissolution−reprecipitation mechanism across the range of our system conditions.

The yield and physical properties of the boehmite product was found to be sensitive to the hydrothermal treatment temperature and the Al/OH^- ratio, controlled by the loading of gibbsite with respect to NaOH. When the initial gibbsite precursor concentration was higher than 0.064 M and the ratio of gibbsite to NaOH was larger than 0.64, dissolution of the gibbsite releases sufficient concentrations of aluminate ions that reach a saturation state that overcomes the nucleation barrier to precipitate boehmite. But higher ratios of gibbsite to NaOH, such as 3.2, are found to slow the phase transformation, leaving residual unreacted gibbsite in the final product for our chosen run duration. Higher temperatures appear to improve the phase transformation rate but also typically yield smaller-sized boehmite particles.

ASSOCIATED CONTENT

Supporting Information

The Supporting Information is available free of charge on the ACS Publications website at DOI: 10.1021/acs.cgd.9b00468.

DOI: 10.1021/acs.cgd.9b00468
Cryst. Growth Des. 2019, 19, 5557−5567

AFM images, XRD patterns of boehmite samples synthesized at different conditions; AFM image of sample collected at 6 h hydrothermal treatment time; table of the fitting results of Figure 10; and overview of boehmite synthesis conditions and resulting products with secondary Al(III) precursor and/or organic additives (PDF)

AUTHOR INFORMATION

Corresponding Authors

*E-mail: xin.zhang@pnnl.gov (X.Z.).
*E-mail: kevin.rosso@pnnl.gov (K.M.R.).

ORCID

Xin Zhang: 0000-0003-2000-858X
Jian Zhi Hu: 0000-0001-8879-747X
Hsiu-Wen Wang: 0000-0002-2802-4122
Chuan Wan: 0000-0002-8226-7619
Nicholas R. Jaegers: 0000-0002-9930-7672
Carolyn I. Pearce: 0000-0003-3098-1615
Kevin M. Rosso: 0000-0002-8474-7720

Notes

The authors declare no competing financial interest.

ACKNOWLEDGMENTS

This work was supported by IDREAM (Interfacial Dynamics in Radiation Environments and Materials), an Energy Frontier Research Center funded by the U.S. Department of Energy (DOE), Office of Science, Basic Energy Sciences (BES). A portion of this research was performed using the Environmental Molecular Sciences Laboratory, a national scientific user facility sponsored by the DOE Office of Biological and Environmental Research and located at PNNL. PNNL is a multiprogram national laboratory operated for the DOE by Battelle Memorial Institute under Contract No. DE-AC05-76RL01830.

REFERENCES

(1) Trueba, M.; Trasatti, S. P. γ-Alumina as a Support for Catalysts: A Review of Fundamental Aspects. *Eur. J. Inorg. Chem.* **2005**, *2005*, 3393−3403.
(2) Liu, Q.; Wang, A.; Wang, X.; Gao, P.; Wang, X.; Zhang, T. Synthesis, characterization and catalytic applications of mesoporous γ-alumina from boehmite sol. *Microporous Mesoporous Mater.* **2008**, *111*, 323−333.
(3) Granados-Correa, F.; Jimenez-Becerril, J. Chromium (VI) adsorption on boehmite. *J. Hazard. Mater.* **2009**, *162*, 1178−84.
(4) Li, P.; Zheng, S.; Qing, P.; Chen, Y.; Tian, L.; Zheng, X.; Zhang, Y. The vanadate adsorption on a mesoporous boehmite and its cleaner production application of chromate. *Green Chem.* **2014**, *16*, 4214−4222.
(5) Zhang, H.; Li, P.; Wang, Z.; Zhang, X.; Zheng, S.; Zhang, Y. In Situ Synthesis of γ-AlOOH and Synchronous Adsorption Separation of V(V) from Highly Concentrated Cr(VI) Multiplex Complex solutions. *ACS Sustainable Chem. Eng.* **2017**, *5*, 6674−6681.
(6) Zhang, J.; Ji, Q.; Zhang, P.; Xia, Y.; Kong, Q. Thermal stability and flame-retardancy mechanism of poly(ethylene terephthalate)/boehmite nanocomposites. *Polym. Degrad. Stab.* **2010**, *95*, 1211−1218.
(7) Esposito Corcione, C.; Manno, R.; Frigione, M. Sunlight-curable boehmite/siloxane-modified methacrylic based nanocomposites as insulating coatings for stone substrates. *Prog. Org. Coat.* **2016**, *95*, 107−119.
(8) Liu, H.; Deng, J.; Li, W. Synthesis of Nickel Nanoparticles Supported on Boehmite for Selective Hydrogenation of p-Nitrophenol and p-Chloronitrobenzene. *Catal. Lett.* **2010**, *137*, 261−266.
(9) Mirzaee, M.; Bahramian, B.; Gholizadeh, J.; Feizi, A.; Gholami, R. Acetylacetonate complexes of vanadium and molybdenum supported on functionalized boehmite nano-particles for the catalytic epoxidation of alkenes. *Chem. Eng. J.* **2017**, *308*, 160−168.
(10) Bai, X.; Caputo, G.; Hao, Z.; Freitas, V. T.; Zhang, J.; Longo, R. L.; Malta, O. L.; Ferreira, R. A.; Pinna, N. Efficient and tuneable photoluminescent boehmite hybrid nanoplates lacking metal activator centres for single-phase white LEDs. *Nat. Commun.* **2014**, *5*, 5702.
(11) Majzlan, J.; Navrotsky, A.; Casey, W. H. Surface enthalpy of boehmite. *Clays Clay Miner.* **2000**, *48*, 699−707.
(12) Hind, A. R.; Bhargava, S. K.; Grocott, S. C. The surface chemistry of Bayer process solids: a review. *Colloids Surf., A* **1999**, *146*, 359−374.
(13) Peterson, R. A.; Buck, E. C.; Chun, J.; Daniel, R. C.; Herting, D. L.; Ilton, E. S.; Lumetta, G. J.; Clark, S. B. Review of the Scientific Understanding of Radioactive Waste at the U.S. DOE Hanford Site. *Environ. Sci. Technol.* **2018**, *52*, 381−396.
(14) Reynolds, J. G.; Cooke, G. A.; Herting, D. L.; Warrant, R. W. Evidence for Dawsonite in Hanford high-level nuclear waste tanks. *J. Hazard. Mater.* **2012**, *209−210*, 186−92.
(15) Chatterjee, S.; Conroy, M. A.; Smith, F. N.; Jung, H.-J.; Wang, Z.; Peterson, R. A.; Huq, A.; Burtt, D. G.; Ilton, E. S.; Buck, E. C. Can Cr(iii) substitute for Al(iii) in the structure of boehmite? *RSC Adv.* **2016**, *6*, 107628−107637.
(16) Huestis, P.; Pearce, C. I.; Zhang, X.; N'Diaye, A. T.; Rosso, K. M.; LaVerne, J. A. Radiolytic stability of gibbsite and boehmite with adsorbed water. *J. Nucl. Mater.* **2018**, *501*, 224−233.
(17) Conroy, M.; Soltis, J. A.; Wittman, R. S.; Smith, F. N.; Chatterjee, S.; Zhang, X.; Ilton, E. S.; Buck, E. C. Importance of interlayer H bonding structure to the stability of layered minerals. *Sci. Rep.* **2017**, *7*, 13274.
(18) Gong, X.; Nie, Z.; Qian, M.; Liu, J.; Pederson, L. A.; Hobbs, D. T.; McDuffie, N. Gibbsite to boehmite transformation in strongly caustic and nitrate environments. *Ind. Eng. Chem. Res.* **2003**, *42*, 2163−2170.
(19) Sonthalia, R.; Behara, P.; Kumaresan, T.; Thakre, S. Review on alumina trihydrate precipitation mechanisms and effect of Bayer impurities on hydrate particle growth rate. *Int. J. Miner. Process.* **2013**, *125*, 137−148.
(20) Zhang, X.; Zhang, X.; Graham, T. R.; Pearce, C. I.; Mehdi, B. L.; N'Diaye, A. T.; Kerisit, S.; Browning, N. D.; Clark, S. B.; Rosso, K. M. Fast Synthesis of Gibbsite Nanoplates and Process Optimization using Box-Behnken Experimental Design. *Cryst. Growth Des.* **2017**, *17*, 6801−6808.
(21) Sipos, P. The structure of Al(III) in strongly alkaline aluminate solutions — A review. *J. Mol. Liq.* **2009**, *146*, 1−14.
(22) Pouvreau, M.; Dembowski, M.; Clark, S. B.; Reynolds, J. G.; Rosso, K. M.; Schenter, G. K.; Pearce, C. I.; Clark, A. E. Ab Initio Molecular Dynamics Reveal Spectroscopic Siblings and Ion Pairing as New Challenges for Elucidating Prenucleation Aluminum Speciation. *J. Phys. Chem. B* **2018**, *122*, 7394−7402.
(23) Watling, H. R.; Fleming, S. D.; van Bronswijk, W.; Rohl, A. L. Ionic structure in caustic aluminate solutions and the precipitation of $Al(OH)_3$. *J. Chem. Soc., Dalton Trans.* **1998**, *1998*, 3911−3917.
(24) Hu, J. Z.; Zhang, X.; Jaegers, N. R.; Wan, C.; Graham, T. R.; Hu, M.; Pearce, C. I.; Felmy, A. R.; Clark, S. B.; Rosso, K. M. Transitions in Al Coordination during Gibbsite Crystallization Using High-Field 27Al and 23Na MAS NMR Spectroscopy. *J. Phys. Chem. C* **2017**, *121*, 27555−27562.
(25) Zhang, X.; Cui, W.; Page, K. L.; Pearce, C. I.; Bowden, M. E.; Graham, T. R.; Shen, Z.; Li, P.; Wang, Z.; Kerisit, S. N.; N'Diaye, A. T.; Clark, S. B.; Rosso, K. M. Size and Morphology Controlled Synthesis of Boehmite Nanoplates and Crystal Growth Mechanisms. *Cryst. Growth Des.* **2018**, *18*, 3596−3606.

DOI: 10.1021/acs.cgd.9b00468
Cryst. Growth Des. 2019, 19, 5557−5567

(26) Lopushan, V. I.; Kuznetsov, G. F.; Pletnev, R. N.; Kleshev, D. G. Kinetics of phase transitions of gibbsite during heat treatment in air and in water vapor. *Refract. Ind. Ceram.* **2007**, *48*, 378−382.
(27) Parkhurst, D. L. User's guide to PHREEQC: A computer program for speciation, reaction-path, advective-transport, and inverse geochemical calculations; *U.S. Geological Survey Water-Resources Investigations Report 95-4227*; U.S. Geological Survey: Reston, VA, 1995.
(28) Graham, T. R.; Dembowski, M.; Martinez-Baez, E.; Zhang, X.; Jaegers, N. R.; Hu, J.; Gruszkiewicz, M. S.; Wang, H. W.; Stack, A. G.; Bowden, M. E.; Delegard, C. H.; Schenter, G. K.; Clark, A. E.; Clark, S. B.; Felmy, A. R.; Rosso, K. M.; Pearce, C. I. In Situ (27)Al NMR Spectroscopy of Aluminate in Sodium Hydroxide Solutions above and below Saturation with Respect to Gibbsite. *Inorg. Chem.* **2018**, *57*, 11864−11873.
(29) Bénézeth, P.; Hilic, S.; Palmer, D. A. The Solubilities of Gibbsite and Bayerite Below 100 °C in Near Neutral to Basic Solutions. *J. Solution Chem.* **2016**, *45*, 1288−1302.
(30) Wesolowski, D. J. Aluminum speciation and equilibria in aqueous solution: I. The solubility of gibbsite in the system Na-K-Cl-OH-Al $(OH)_4$ from 0 to 100 C. *Geochim. Cosmochim. Acta* **1992**, *56*, 1065−1091.
(31) Xiong, Y. A Pitzer model for the Na−Al$(OH)_4$−Cl−OH system and solubility of boehmite (AlOOH) to high ionic strength and to 250°C. *Chem. Geol.* **2014**, *373*, 37−49.
(32) Königsberger, E.; May, P. M.; Hefter, G. Comprehensive Model of Synthetic Bayer Liquors. Part 3. Sodium Aluminate Solutions and the Solubility of Gibbsite and Boehmite. *Monatsh. Chem.* **2006**, *137*, 1139−1149.
(33) Palmer, D. A.; Bénézeth, P.; Wesolowski, D. J. Aqueous high-temperature solubility studies. I. The solubility of boehmite as functions of ionic strength (to 5 molal, NaCl), temperature (100−290 C), and pH as determined by in situ measurements. *Geochim. Cosmochim. Acta* **2001**, *65*, 2081−2095.
(34) Bénézeth, P.; Palmer, D. A.; Wesolowski, D. J. Aqueous high-temperature solubility studies. II. The solubility of boehmite at 0.03 m ionic strength as a function of temperature and pH as determined by in situ measurements. *Geochim. Cosmochim. Acta* **2001**, *65*, 2097−2111.
(35) Prange, M. P.; Zhang, X.; Bowden, M. E.; Shen, Z.; Ilton, E. S.; Kerisit, S. N. Predicting Surface Energies and Particle Morphologies of Boehmite (γ-AlOOH) from Density Functional Theory. *J. Phys. Chem. C* **2018**, *122*, 10400−10412.
(36) Mishra, D.; Anand, S.; Panda, R. K.; Das, R. P. Hydrothermal Preparation and Characterization of Boehmites. *Mater. Lett.* **2000**, *42*, 38−45.
(37) Chen, X. Y.; Huh, H. S.; Lee, S. W. Hydrothermal synthesis of boehmite (γ-AlOOH) nanoplatelets and nanowires: pH-controlled morphologies. *Nanotechnology* **2007**, *18*, 285608.
(38) He, T.; Xiang, L.; Zhu, S. Different nanostructures of boehmite fabricated by hydrothermal process: effects of pH and anions. *CrystEngComm* **2009**, *11*, 1338−1342.
(39) Alemi, A.; Hosseinpour, Z.; Dolatyari, M.; Bakhtiari, A. Boehmite (γ-AlOOH) nanoparticles: Hydrothermal synthesis, characterization, pH-controlled morphologies, optical properties, and DFT calculations. *Phys. Status Solidi B* **2012**, *249*, 1264−1270.
(40) Denigres Filho, R. W. N.; Rocha, G. d. A.; Montes, C. R.; Vieira-Coelho, A. C. Synthesis and Characterization of Boehmites Obtained from Gibbsite in Presence of Different Environments. *Mater. Res.* **2016**, *19*, 659−668.
(41) Zhang, X.; Huestis, P. L.; Pearce, C. I.; Hu, J. Z.; Page, K.; Anovitz, L. M.; Aleksandrov, A. B.; Prange, M. P.; Kerisit, S.; Bowden, M. E.; Cui, W.; Wang, Z.; Jaegers, N. R.; Graham, T. R.; Dembowski, M.; Wang, H.-W.; Liu, J.; N'Diaye, A. T.; Bleuel, M.; Mildner, D. F. R.; Orlando, T. M.; Kimmel, G. A.; La Verne, J. A.; Clark, S. B.; Rosso, K. M. Boehmite and Gibbsite Nanoplates for the Synthesis of Advanced Alumina Products. *ACS Appl. Nano Mater.* **2018**, *1*, 7115−7128.
(42) Wang, S.; Johnston, C. T. Assignment of the structural OH stretching bands of gibbsite. *Am. Mineral.* **2000**, *85*, 739−744.
(43) Ruan, H. D.; Frost, R. L.; Kloprogge, J. T. Comparison of Raman spectra in characterizing gibbsite, bayerite, diaspore and boehmite. *J. Raman Spectrosc.* **2001**, *32*, 745−750.
(44) Wright, A.; Gabaldon, J.; Burckel, D. B.; Jiang, Y. B.; Tian, Z. R.; Liu, J.; Brinker, C. J.; Fan, H. Hierarchically organized nanoparticle mesostructure arrays formed through hydrothermal self-assembly. *Chem. Mater.* **2006**, *18*, 3034−3038.
(45) Wang, Z.; Bian, K.; Nagaoka, Y.; Fan, H.; Cao, Y. C. Regulating Multiple Variables To Understand the Nucleation and Growth and Transformation of PbS Nanocrystal Superlattices. *J. Am. Chem. Soc.* **2017**, *139*, 14476−14482.
(46) Fan, H.; Gabaldon, J.; Brinker, C. J.; Jiang, Y. B. Ordered nanocrystal/silica particles self-assembled from nanocrystal micelles and silicate. *Chem. Commun.* **2006**, *2006*, 2323−2325.

DOI: 10.1021/acs.cgd.9b00468
Cryst. Growth Des. 2019, 19, 5557−5567